Analysis of the effects of control strategies and wave climates on the loading and performance of a laboratory scale horizontal axis tidal turbine

Rodrigo Martinez[a,*], Stephanie Ordonez-Sanchez[a], Matthew Allmark[b], Catherine Lloyd[b], Tim O'Doherty[b], Gregory Germain[c], Benoit Gaurier[c], Cameron Johnstone[a]

[a] *Energy Systems Research Unit, Department of Mechanical and Aerospace Engineering, University of Strathclyde, 75 Montrose St. Glasgow, G1 1XQ*
[b] *Cardiff Marine Energy Research Group, College of Physical Sciences and Engineering, Cardiff University, The Parade, Cardiff, CF24 3AA*
[c] *IFREMER, Marine and Structures Laboratory, Centre Manche Mer du Nord, 150 Quai Gambetta, 62200, Boulogne-sur-Mer*

Abstract

To understand the influence of complex hydrodynamic loads on tidal turbines, laboratory testing is necessary as a first approach. Previous laboratory work undertaken gave an indication that the use of speed control strategies may disguise the associated loading range that a turbine may be subjected to when this is operated with a variable speed control strategy. However, the preceding work was undertaken in a highly controlled environment without the influence of turbulent flows. The focus of this paper is directed towards the study of wave-induced loads on tidal turbines when these are controlled using two strategies and the impact that these parameters have on the turbine's performance when this is operated in a recirculating flume. Laboratory tests were undertaken with a 0.9 m diameter horizontal axis tidal turbine subjected to combined wave and current conditions with both regular and irregular waves. Constant speed and constant torque control strategies have been considered, for which rotor thrust, torque and blade root bending moment have been measured. Results show that similar to previous studies, average loads and power capture values

*Corresponding author
Email address: r.martinez@strath.ac.uk (Rodrigo Martinez)

remain unchanged between control strategies and the superposition of waves to the current. However, signal fluctuations are 2 to 3 times higher for torque control than for constant speed control strategy. A phase difference between the periodic signals of the turbine thrust and the incoming waves was also identified, in this case, the phase variation was lower when using torque than speed control. This work thus demonstrates the implication of studying strategies to control a marine converter from early stages of development.
Keywords: Tank testing, torque control, speed control, tidal turbine, wave-current interaction, marine energy

1. Introduction

In real sea conditions, tidal turbines have to withstand complex hydrodynamic loads. This complexity can be attributed in some cases to the combined wave and current nature of the ocean. The current-induced loads have already been studied in the past [1–4], and lately, attention has been given to the effects produced by wave-induced loading on the devices, as seen in [5–12].

The dynamic nature of these loads are responsible for fluctuations on the turbine's torque and thrust loads by up to 2-3 times the average values [5]. These wave-induced fluctuating loads are also the cause of eccentric loading on the drive-train bearings [13] and has a direct effect on the fatigue life of the blades [14]. Understanding these fluctuations could potentially help with the implementation of more efficient power conditioning methods, facilitate the integration of these turbines into the electricity grid [15] and increase the reliability and resilience of these marine converters.

The majority of the real sea states are characterised by irregular waves, meaning that the effect of these wave climates should be studied in detail. However, studies contemplating these sea climates are currently scarce in the literature with only a few studies reported [16–18]. Even more, the majority of the investigations focused on wave-current research at small scale are often characterised by using a speed control strategy to set the operational point of the

scaled prototype. Other studies have also explored the use of innovative transmission approaches and novel control strategies and more specifically control algorithms to mitigate loading [19–21] or to enhance power capture [22, 23] but these have not looked into the effect of combined wave and current conditions.

A first attempt to look at the effects of regular and irregular waves on tidal turbine models working under both speed and torque control strategies at a towing tank was presented in [17, 18]. These studies gave the bases for the present study, which now includes the presence of turbulence and shear flows in combination with regular and irregular waves at a recirculating tank. Therefore, the aim of this study is to understand if features such as load fluctuation magnitudes and load phasing in more realistic flows are comparable to those that have been quantified at more controlled environments; i.e. tow tanks.

2. Experimental set-up

The turbine was mounted on a 0.105 m diameter stanchion connected to a supporting structure above the 4 x 2 x 18 m wave and current flume of IFREMER as seen in Figure 1 [24]. The turbine was mounted 1 m below the water surface, and centred in the cross stream direction, at 2 m from the side walls (Figure 1b).

The tank setup for the turbine and characterisation tests is shown in Figure 2. The flow speed was measured with an Laser Doppler Velocimeter (LDV) mounted 1 m upstream of the turbine at different vertical positions and an Acoustic Doppler Velocimeter (ADV) was mounted 1 m below the water surface in line with the rotor plane 1.05 m from the centre of the rotor.

Two different wave makers configurations depending on the waves generated have been used: the wave makers submerged at a water depth of 0.3 m and 0.5 m.

The wave height was measured with a resistive wave gauge. It was placed in line with the rotor plane at 0.78 m from the centre of the rotor.

An extra set of flow characterisation tests were performed once the turbine

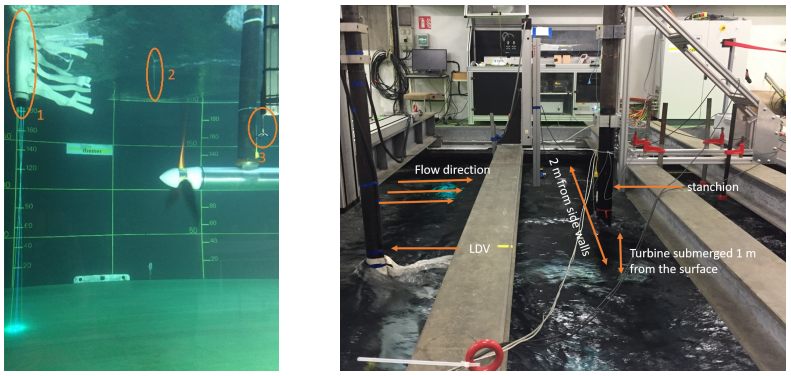

(a) (b)

Figure 1: Figure (a) showing the laser Doppler velocimeter was placed 1 m upstream of the turbine (1), a wave gauge (2) was installed in line with the turbine and with an acoustic Doppler velocimeter (3) on the opposite side. The current flowed left to right as pointed out in (b).

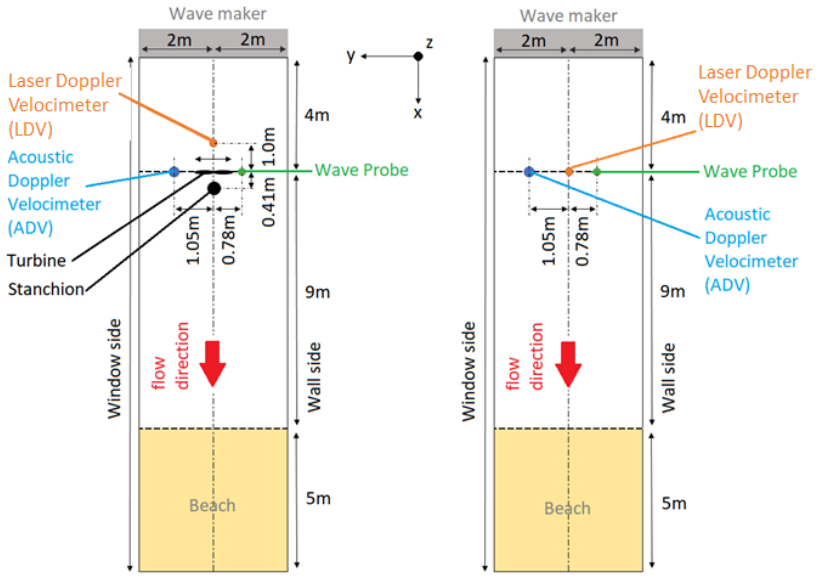

Figure 2: Top view of tank setup during turbine testing (left) and flow characterisation tests with the turbine removed (right).

was removed from the tank. In this case, the LDV position was moved to the rotor plane (Figure 2 right).

2.1. Turbine model

The turbine used in this experiments was a three-bladed, horizontal axis turbine with a 0.9 m diameter at a $1/20^{th}$ scale. This scales geometrically to a typical 18 m full-scale tidal turbine. Detail on the development of this model can be found in [25]. A Bosch Rexroth motor/drive system was used to control the turbine using an encoder feedback for servo-control. The turbine control algorithms were integrated in the Programmable Logic Controller (PLC) associated with the drive system and supplied by Bosch Rexroth [25].

The blade profile design was based on a Wortmann FX 63-137 profile. Further information on the blade profile and design can be found in [26–28].

Turbine instrumentation

Rotor torque and thrust signals were logged with an Applied Measurements transducer. The transducer was fitted between the rotor hub and the dynamic seals to avoid recording friction forces from the dynamic seals. The factory calibrated gradient/slope relating electrical signals to loading values was used to infer torque and thrust magnitudes.

The out-of-plane bending moment was logged with strain gauges mounted on each of the blade roots. The strain gauges sets were fitted by Applied Measurements. In this work, only the root bending moment data from one blade is discussed.

Tests where the turbine was stationary and the water was still were performed to record any offset in the instruments readings.

Turbine Control

A major aspect of the research presented was to quantify the effects of two opposing control strategies on the power production and loads measured under the wave cases tested. The two control strategies tested, fixed torque control

and fixed speed control, were both achieved utilising the permanent magnet synchronous machine (PMSM) housed in the turbine nacelle. Each control approach was implemented via a set of motor drives and an embedded PLC. Specifically, the goal of the fixed speed control approach was to utilise the embedded PMSM to maintain a fixed operating rotational velocity for the turbine during the experiments. Conversely, the goal of the fixed torque control case was to maintain a fixed braking torque applied by the integrated PMSM - allowing the turbine to accelerate or decelerate in response to changes in the torque developed by the turbine rotor.

The drive system utilised back-to-back Voltage Source Converters (VSCs) either side of a DC-Bus. The primary interest in terms of turbine control is the operation of the PMSM side VSC which operates as an inverter to maintain the required device winding voltages. The required winding voltages are defined by the various control strategies detailed below. The voltage targets are fed into a Pulse Width Modulator (PWM) which in turn defines the inverter or VSC switching scheme required to achieve the aforementioned target voltages.

The required winding voltages are developed via the torque and speed control loops. Torque control, whereby the drives and PMSM implement a constant braking torque, was undertaken via Vector Oriented Control (VOC). VOC utilises current measurements and rotor position and velocity measurements to maintain the AC current in the PMSM windings to achieve a specified braking torque. The reference currents required to achieve a specific set-point braking torque, which in the direct-quadrature axes (dq) reference frame, are presented in equation 1.

$$\begin{bmatrix} i_{dref} \\ i_{qref} \end{bmatrix} = \begin{bmatrix} 0 \\ \frac{3}{2} \cdot \frac{1}{P \cdot \psi} \end{bmatrix} \tau_{ref} \tag{1}$$

In Equation 1, i_{dref}, i_{qref} are the required direct and quadrature axis currents in Amps, respectively. τ_{ref} is the braking torque set-point for the given test case, P is the number of pole pairs and ψ is the magnetic flux linkage of the permanent magnets of the PMSM rotor in Weber (Wb). Error signals can

be defined as $E_d = i_{dref} - i_d$ and $E_q = i_q ref - i_q$, for the direct and quadrature axes, respectively. The error signals, which define the discrepancy between the actual current in the motor windings and the required current in the motor windings, are generated and input into a PI controller to define the required voltages. The voltage references generated via the PI controller, which are input into the PWM, are defined in Equation 2.

$$\begin{bmatrix} V_{dref} \\ V_{qref} \end{bmatrix} = \begin{bmatrix} E_d & \int E_d \cdot dt & -L_q \cdot i_q \\ E_d & \int E_d \cdot dt & (L_d \cdot i_d + \psi) \end{bmatrix} \begin{bmatrix} K_p \\ K_i \\ \omega \end{bmatrix} \tag{2}$$

In Equation 2 K_p and K_i are the proportional and integral gains, respectively; ω is the rotational speed of the turbine and PMSM in $Rads^{-1}$. The reference voltages, V_{dref} and V_{qref}, are converted into the three phase voltages which are fed into a PWM to generate gate-pulses for the 6-IGBT based VSC.

Speed control, whereby the PMSM attempts to maintain a near constant rotational velocity of the turbine rotor, is achieved by an addition of an outer velocity control loop to the previously described VOC current control loop. This control loop utilises encoder measurements of the rotational velocity of turbine or PMSM to define the following error signal, $E_\omega = \omega_{ref} - \omega$, which is also fed into a PI controller. In this case the error signal defines the discrepancy between the rotor rotational velocity and the target rotational velocity. In this way the output of the speed control PI controller defines the required braking torque required to maintain the ω_{ref} set for the given test. In this way Equation 1 can be altered to give Equation 3 which defines the require winding currents which will develop a PMSM braking torque to minimise the aforementioned discrepancy between the actual and required rotational velocity .

$$\begin{bmatrix} i_{dref} \\ i_{qref} \end{bmatrix} = \begin{bmatrix} 0 \\ \frac{3}{2} \cdot \frac{1}{P \cdot \psi} \end{bmatrix} \left(K_{p\omega} \cdot E_\omega + K_{i\omega} \cdot \int E_\omega \cdot dt \right) \tag{3}$$

In Equation 3, $K_{p\omega}$ and $K_{i\omega}$ are the proportional and integral gains for the speed control loop.

The two control loops were tuned to achieve critical damping. Figure 3 shows a schematic of the setup described, indicating the cascaded loop structure utilised to achieve the two control strategies. It should be noted that for the torque control cases the outer speed control loop is not utilised and the τ_{ref} value in the schematic and in Equation 1 are set directly and not by the output of the speed control loop.

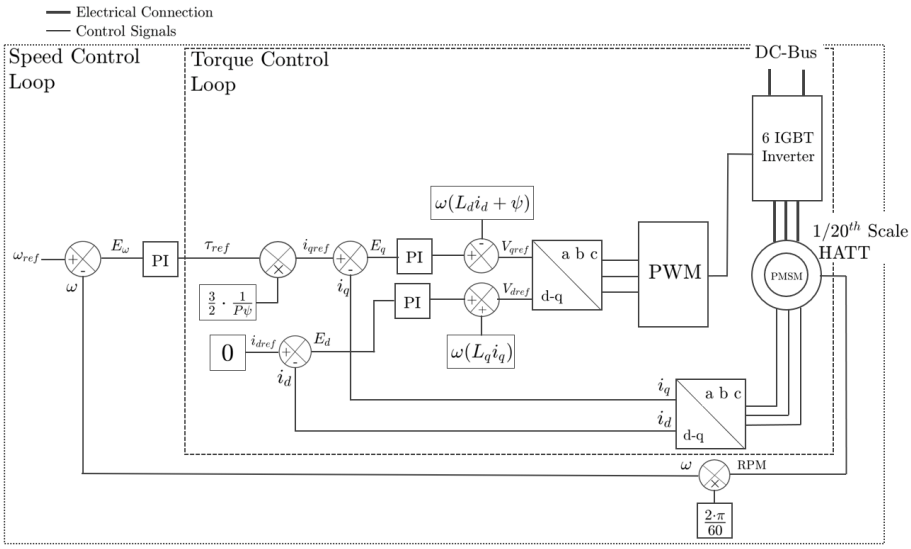

Figure 3: Schematic of the control implementation utilised for speed and torque control of the model HATT.

2.2. Test programme

Flow conditions tested included current-only cases as well as regular and irregular wave-current cases. The current speed was kept constant for each case, and was chosen to provide approximate Reynolds independent conditions based on the blade chord length at 0.7 r/R ($Re_{chord} \approx 6.4 \times 10^4$) [25, 28]. This means that at these conditions the Reynolds Number insensitivity is achieved and therefore all non-dimensional characteristics presented in this research can be considered independently of the Reynolds number, as stated by [29]. Wave parameters were selected to match the ones used in [17] and [18]. The wave

height (H) and wave frequency (F) of the regular waves selected are shown in Table 1. For the irregular wave cases, a JONSWAP spectrum was selected. The irregular waves significant wave height (H_S) and peak wave frequency (F_P) was selected to match with the wave height and wave frequency of the regular waves ($H_S = H$ and $F_P = F$, respectively). Table 1 shows the input test parameters for all cases. The difference between the current cases C1, C2, C3 and C4 is the depth of the wave maker.

All cases have been tested under speed control strategy. Cases C3W3R and C3W3J have also been tested in torque control. The turbine was operated at a range of tip-speed-ratios (TSR) from 0 to 8. TSR is defined as the ratio between the tangential speed of the tip of a blade and the actual speed of the water:

$$TSR = \frac{\omega R}{U} \tag{4}$$

Table 1: Testing matrix used for the experiments

Case	**Wave type**	**Flow speed U [m/s]**	**Wave height H [m]**	**Wave freq. F [Hz]**	**Full scale H [m]**	**Full scale F [Hz]**	**Control strategy**	**Tested at CNR-INM** (see [18])
SC-C1^A	-	1.0	-	-	-	-	Speed	yes
SC-C2^B	-	1.0	-	-	-	-	Speed	no
SC-C2W1R	Regular	1.0	0.11	0.7	2.2	0.15	Speed	no
SC-C3^C	-	1.0	-	-	-	-	Speed	no
SC-C3W2R	Regular	1.0	0.09	0.5	1.8	0.11	Speed	no
SC-C3W3R	Regular	1.0	0.19	0.7	3.8	0.15	Speed	yes
TC-C3W3R	Regular	1.0	0.19	0.7	3.8	0.15	Torque	yes
SC-C3W3J	JONSWAP	1.0	0.19*	0.7#	3.8	0.15	Speed	yes
TC-C3W3J	JONSWAP	1.0	0.19*	0.7#	3.8	0.15	Torque	yes
SC-C4^A	-	1.1	-	-	-	-	Speed	no

^{A}no wave maker mounted

^{B}wave maker at 0.3 m

^{C}wave maker at 0.5 m

*Significant wave height (H_S)

#Peak wave frequency (F_P)

All the data from the turbine's instrumentation and flow measurement instruments was synchronously sampled at 100 Hz.

After this experimental set-up description, the paper is divided into two parts. The first part covers a flow velocity analysis and how this impacts the loading and performance of the turbine. The second part discusses the results measured from the turbine's instrumentation, as time-averaged loading and performance followed by angle-averaged loading, load fluctuations, signal phasing and finally an analysis of the load fluctuations in the frequency domain.

3. Flow analysis and its effects on turbine performance

3.1. Flow velocity characteristics

The LDV data was obtained with and without the turbine in the flume tank. The measurements for when the turbine was not mounted were recorded in the rotor plane. For the cases where the turbine was mounted, the measurements were recorded 1 m upstream of the turbine. In Figure 4, the LDV velocity depth profiles are shown. The dashed lines represent the flow characterisation tests performed with the turbine mounted (TM) and the solid lines represent the flow characterisation with the turbine removed from the tank (FC). There is a small deficit between the TM and FC data. When the turbine is mounted, it slows down the incoming flow up to 1m upstream, where the LDV probe is fixed [30]. At hub height, the presence of the turbine can slow down the flow up to 5% the flow without turbine.

From Figure 4, it is possible to see how the presence and the depth at which the wave maker is mounted influences the flow speed as well. When the wave maker is not mounted (Figure 4a) the flow is closest to the set speed of 1 m/s and 1.1 m/s, respectively. When the wave maker is mounted at a depth of 0.3 m (Figure 4b), a velocity profile starts to develop with the flow speed beginning to slow towards the top section of the water column while a decrease in flow velocity is noticeable in the central and lower sections of the water column. Finally, when the wave maker is mounted at a depth of 0.5 m (Figure 4c), the

flow is far from the set point and the biggest change in velocity profile was observed. At the top section of the water column, the flow speed is up to 23% slower than at the bottom section. The mounting depth of the wave makers represent an approximate blockage of the tank's cross-section of 15% for the 0.3 m depth and 25% for the 0.5 m depth.

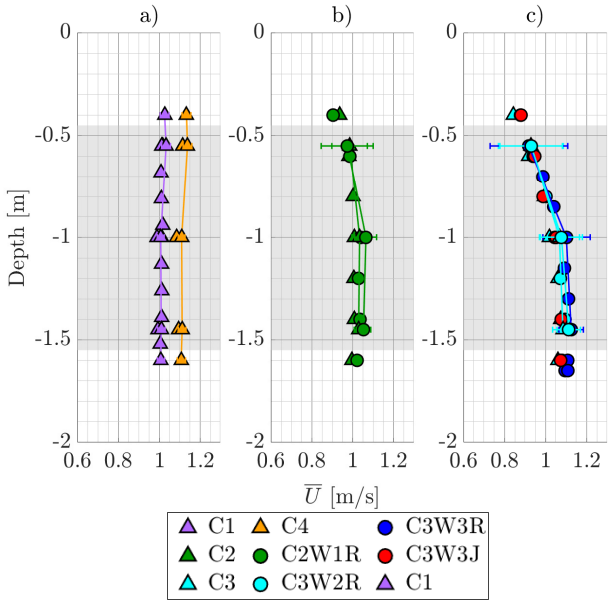

Figure 4: Comparison of flow velocity depth profiles with error bars using the LDV data. The dashed lines are 1 m upstream of the turbine (TM). The solid lines correspond to the measurements taken at the rotor plane (no turbine mounted) (FC). The greyed area represents the rotor's position within the water column and for each of the following cases: a) C3 and C4 cases, b) C1 cases, c) C2 cases.

The turbulence intensity (TI) depth profiles (Figure 5) present a high variability for the cases where the wave maker was installed. The TI goes from a steady 2% across the water column when the wave maker is not mounted (Figure 5a), to a curve increasing in TI towards the top of the water column to a value close to 20% (Figure 5c), showing the effect of the wave maker on the flow characteristics.

Comparing the flow characterisation tests with real sea data, Figure 6a shows

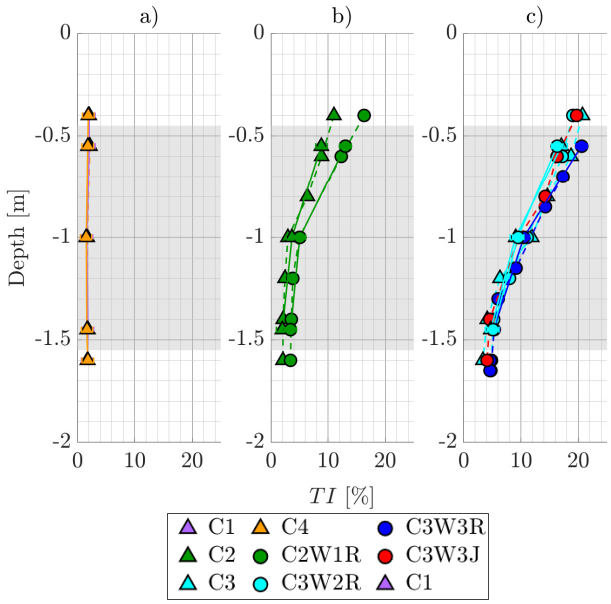

Figure 5: Comparison of turbulence intensity (TI) depth profiles with LDV. The dashed lines correspond to the measurements taken at 1 m upstream of the turbine (TM) and the solid lines to those obtained at the rotor plane (no turbine mounted) (FC). The greyed area represents the rotor's position within the water column and for each of the following cases: a) C3 and C4 cases, b) C1 cases, c) C2 cases.

four velocity depth profiles from the west coast of the UK at the same location at different times of the year. A $1/8^{th}$ power law approximation is added for reference. When comparing Figure 4c with Figure 6a, it is clear that features of the flow velocity in the laboratory and in the ocean are inverted. Similarly, the TI shows no similar trendlines for both locations, the west coast of the UK site (Figure 6b) and the tank the wave makers (Figure 5c). Even if the site presented here follows more appropriately an $1/8^{th}$ power law approximation instead of a $1/7^{th}$ power law which is a common practice [31–33]; it has been proved by [34] that a power law of $1/8^{th}$ has no significant effect on the turbine performance.

The non-dimensional coefficients that measure the thrust and power generated by the rotor are given by:

$$C_T = \frac{T}{\frac{1}{2} \cdot \rho \cdot A \cdot \overline{U_0^2}} \tag{5}$$

$$C_P = \frac{P}{\frac{1}{2} \cdot \rho \cdot A \cdot \overline{U_0^3}} \tag{6}$$

where P is the power generated, T is the rotor thrust, ρ is the water density, A is the rotor area and U_0 is the spatial average of the flow measurements done within the rotor area. The average and instantaneous power is quantified using Equation 7:

$$P = \tau \cdot \omega \tag{7}$$

where τ relates to the rotor torque. τ and ω are derived from an encoder and a torque transducer, respectively. In this study, either the speed or torque remain stationary, at some extent, depending on the control strategy employed.

3.2. Wave characteristics

For the regular waves, average wave heights of 0.17, 0.12 and 0.08 m were calculated with the zero-up crossing method for the cases C3W3R, W2-C1 and W3-C2, respectively. An average wave height standard deviation of 0.002 m

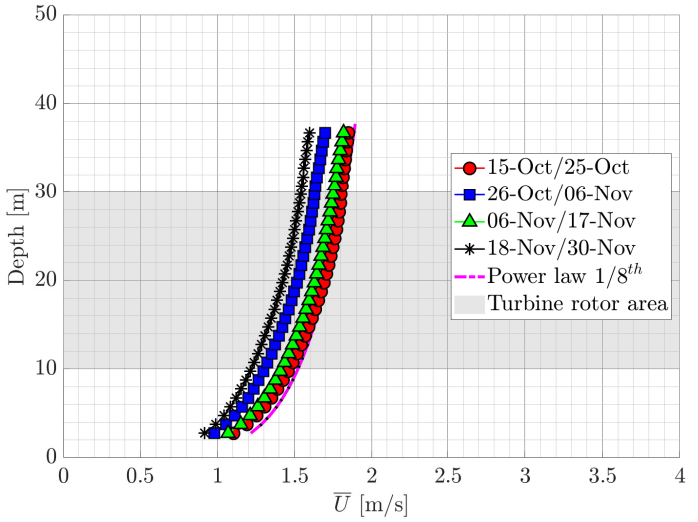

(a)

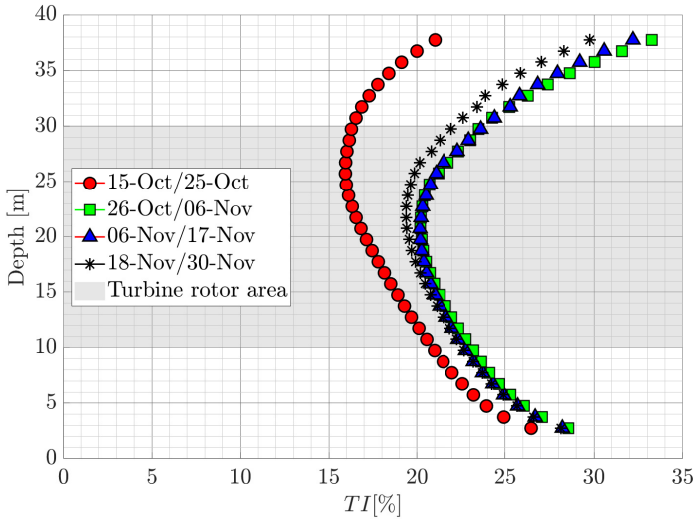

(b)

Figure 6: ADCP data from the west coast of the UK at different dates. a) velocity depth profiles and a $1/8^{th}$ power law approximation for reference, b) TI depth profiles.

between tests was recorded for all regular wave cases. The average wave frequency for cases C3W3R and W2-C1 was 0.69 Hz and 0.50 Hz for case W3-C2. Respective wave frequency standard deviations of 0.0001, 0.00005 and 0.0076 Hz between tests were observed.

For the irregular wave tests, the zero up-crossing method was used to define and calculate the wave height and period of each of the waves throughout the time series.

According to the flow conditions selection criteria presented in Section 2.2, the significant wave height of the irregular wave cases should be equal to the average wave height of the C3W3R (0.19 m) case ($H_S = H$). Similarly, the peak wave frequency of the irregular wave cases (0.68 Hz) should be equal to the average wave frequency of the C3W3R (0.7 Hz) case ($F_P = F$). Figure 7 shows the power spectra density of wave height for all a) regular (C3W3R) and b) irregular (C3W3J) wave cases available. It can be seen that the largest peaks in both figures fall very close to each other. As shown in Table 2, the wave height criteria did not match. However, the frequency criteria had a very good match. Perhaps, the duration of the tests did not allow for the wave spectrum to fully develop.

Table 2: Average values between repeat tests of wave parameters for all regular (C3W3R) and irregular (C3W3J) wave cases available using zero up-crossing method

Metric		**C3W3R**	**C3W3J**
Duration	[s]	200	300
f	[Hz]	0.70	N/A
f_P^*	[Hz]	N/A	0.68
H	[m]	0.17	0.06
σH	[m]	0.018	0.027
H_S	[m]	N/A	0.09
σH_S	[m]	N/A	0.017

*taken from Figure 7

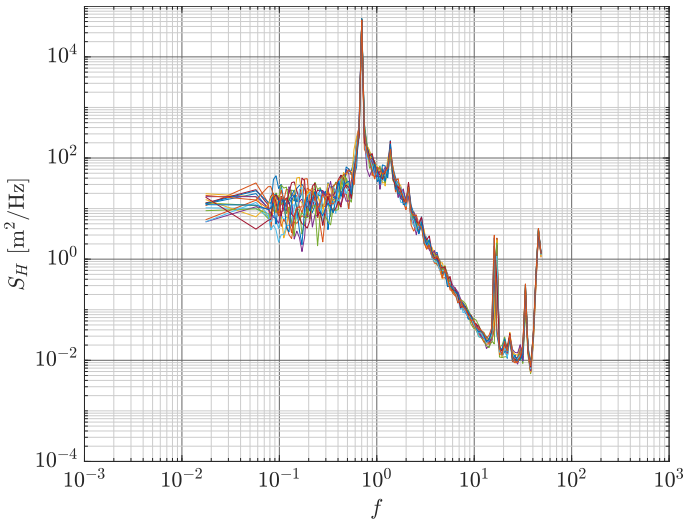

(a)

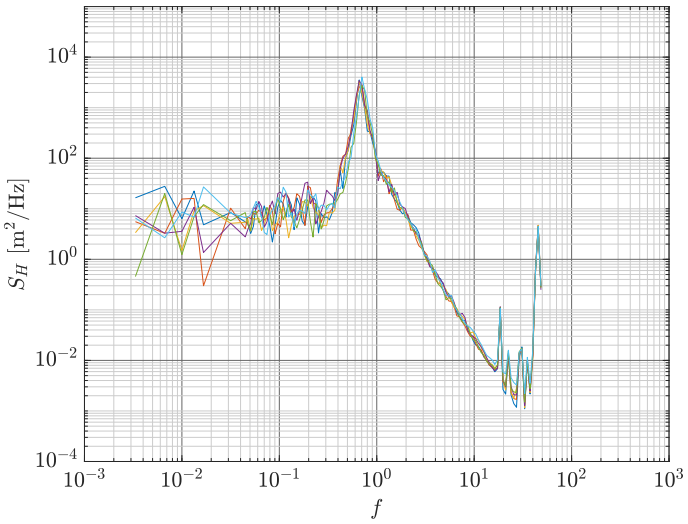

(b)

Figure 7: Power spectra density of wave height for all a) regular (C3W3R) and b) irregular (C3W3J) wave cases available

4. Waves effects on turbine performance

4.1. Average loading and performance

The turbine's C_P is shown in Figure 8 for all flow conditions and control modes. A reduction is seen for the current-only case SC-C1 at 1.0 m/s and no wave maker installed.

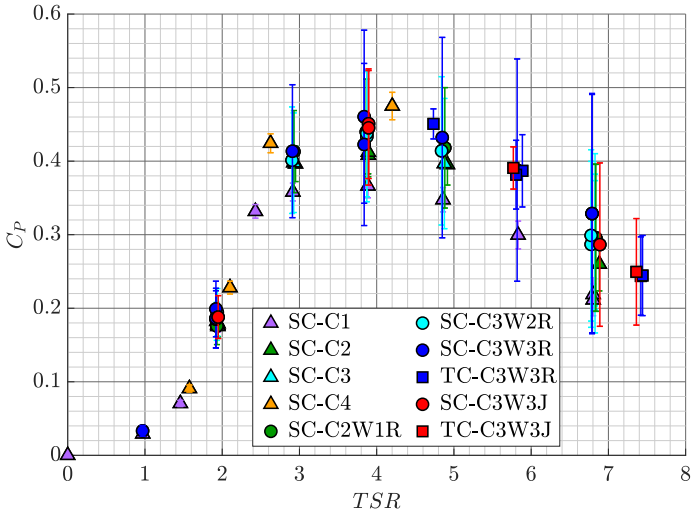

Figure 8: Mean power coefficient (C_P) with SD error bars on all points against tip-speed-ratio (TSR) for all cases.

In Figures 9, the variation of C_T with TSR is plotted. The C_T presents a similar behaviour than the C_P for $TSR \geq 4$, where the C_T for case SC-C1 progressively decreases up to 10% from the other cases.

The data for blade 3's root bending moment ($RBM3$) for all the cases against TSR is shown in Figure 10. In this case, a difference of about 15% between the highest velocity case (SC-C4), the highest waves cases (C3W3R) and the rest of the cases can be seen at $TSR \geq 4$.

The agreement observed between the different cases in Figures 8-10 indicated that neither the control mode nor the addition of either regular or irregular waves had a significant influence in the average values of C_P, C_T nor RBM, as previously reported in [17] and [18].

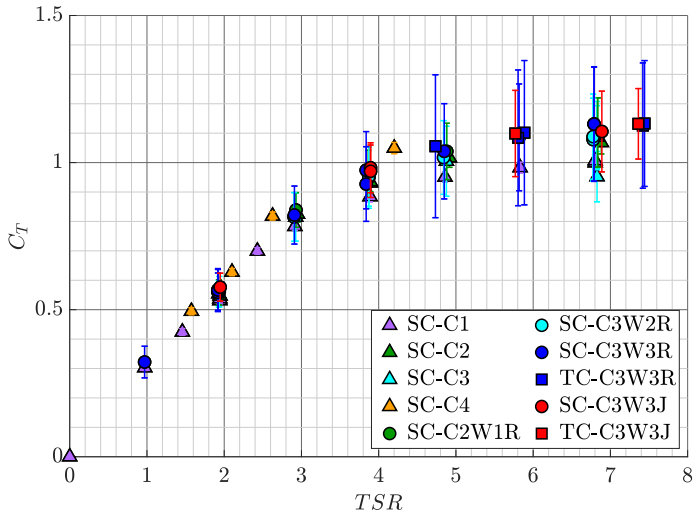

Figure 9: Mean thrust coefficient (C_T) with SD error bars on all points against tip-speed-ratio (TSR) for all cases.

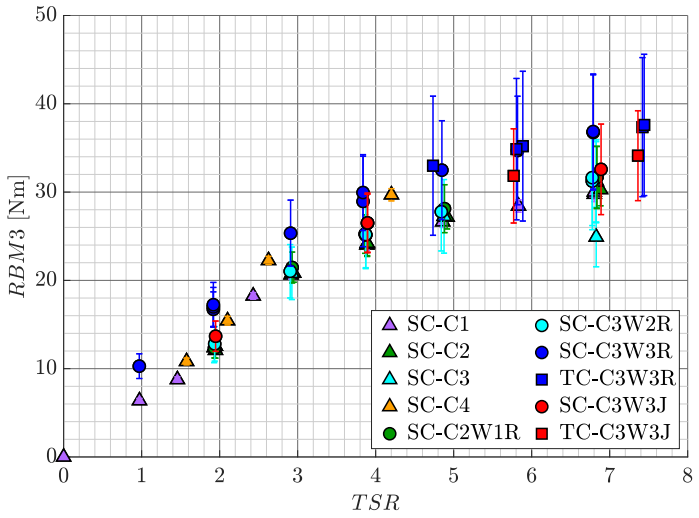

Figure 10: Mean root bending moment (RBM) of blade 3 with SD error bars on all points against tip-speed-ratio (TSR) for all cases.

4.2. Angle averaged loading

In order to understand the loading dependency on the rotor's angular position, with the aid of the encoder, the loading were averaged by 1° bins. Figure 11 shows the front view of the rotor with the blades, stanchion (or supporting mast) and the rotational direction identified. All polar plots in this section use this view as a reference.

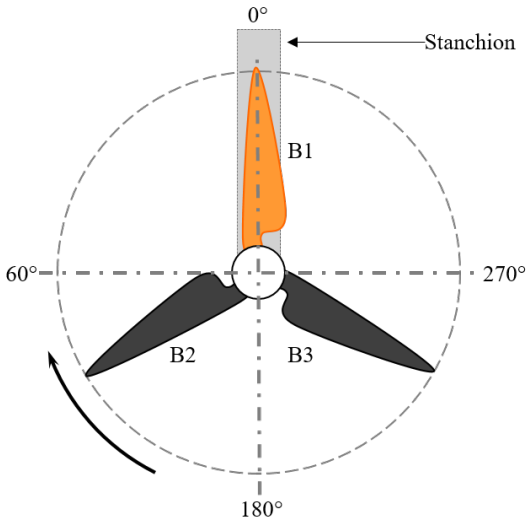

Figure 11: Front view of the rotor identifying the blades, the stanchion and rotational direction. This schematic is used when analysing polar plots.

Figure 12 shows the angle-averaged RBM data for current-only case SC-C3 and wave case SC-C3W3R. In both cases, there is an angular shift at $TSR = 2$. This behaviour could be associated to the slope that happens just before τ_{MAX} at $TSR \approx 3$.

Figure 13 explores the influence of the wave makers' presence on the thrust data. The data for cases SC-C2 and SC-C3, both with the wave makers installed, present a three-lobed shape. The case with no wave maker installed (SC-C1) shows a smaller variation range with the three-lobed shape not as well defined as in the other cases. The smaller lobe is located in the region $0° - 240°$ for all cases. The vertical elongated shape of the curves could be associated to the

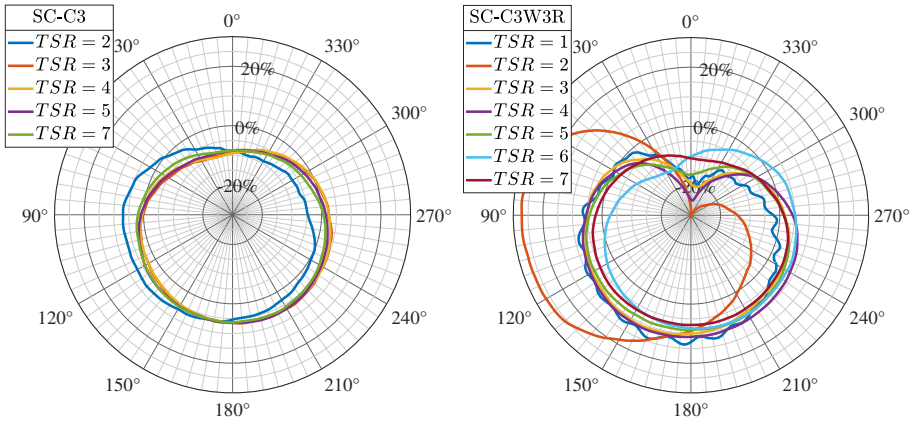

Figure 12: Angle averaged $RBM$for a) current-only case SC-C3 and b) regular wave case SC-C3W3R for $TSR = 1 - 7$. Both figures use the same radius range for ease of comparison

velocity depth profiles shown in Section 3.

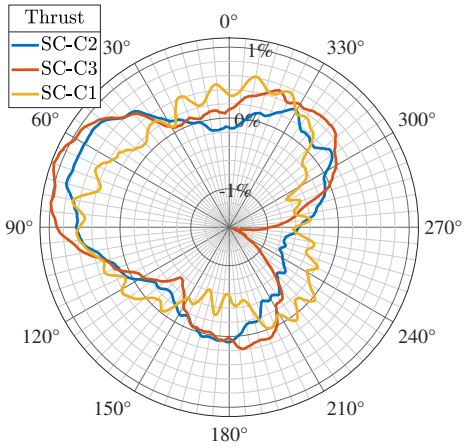

Figure 13: Angle averaged thrust for current-only cases in speed control at $TSR = 4$

In Figure 14, the polar data of the root bending moment (RBM) for blade 2 is plotted. As a reference, the stanchion is situated on the line between the centre of the plot and the 0° tick, as seen in Figure 11. The data for the cases of $TSR = 5$ and $TSR = 7$ are shown in Figure 14a and b, respectively. The upward facing notch seen in both figures is associated to the tower shadow effect. This

tower shadow effect, although small, has an influence in the loading depending on the angular position of each blade. It can be seen that the notch is not completely vertical but a lag can be seen as it was experienced in [35–38]. This lag can also be seen on the thrust curves from Figure 13. The eccentricity seen in this figures will be transmitted to the rotor shaft and consideration should be taken when designing mechanical components. The eccentricity that each of the blades produce is reflected on the thrust curves and the particular three-lobed shape observed in each of them.

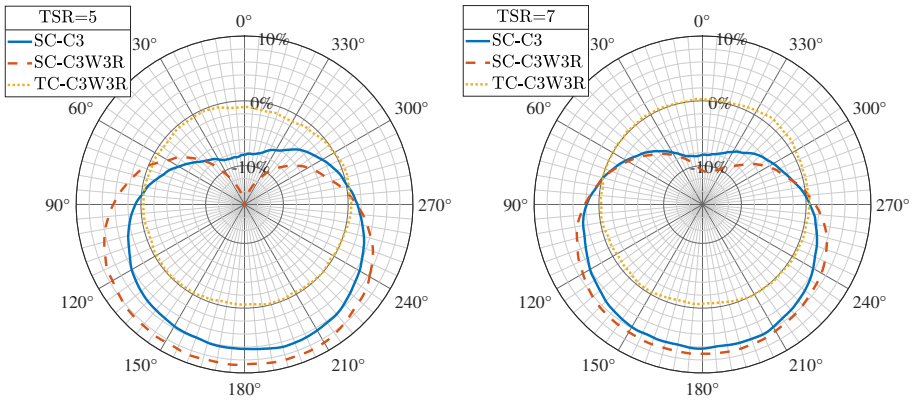

Figure 14: Front view of the rotor with angle averaged $RBMs$ for cases SC-C3, SC-C3W3R and TC-C3W3R. a) $TSR = 5$ b) $TSR = 7$. Shown as a percentage of the averaged values.

Figure 15 shows the angle-averaged rotational speed (a,b) and torque (c,d) and compares them between regular (a,c) and irregular waves (b,d) in both control modes. The polar plots represent the front view of the rotor with the stanchion located on the line between the centre at 0° (refer to Figure 11). Under torque control (TC), the oscillations on the rotational speed (top figures) under regular waves (a) are higher than under irregular waves (b). For both wave conditions, the fluctuations between control modes is highly observable.

The bottom figures show the torque under both control strategies. Under torque control, the torque signal fluctuations remained close to 0% off the mean value. Under speed control (SC), the torque has larger fluctuations but with

lower frequency. The shape of the torque's behaviour from W3 is similar to the thrust behaviour seen in Figure 16. The difference between the torque behaviour under speed control between wave conditions (orange data on Figures 15c and 15d) could be associated to the random nature of the irregular waves and the fact that the maximum wave height of the irregular case is lower than the average wave height of the regular wave case.

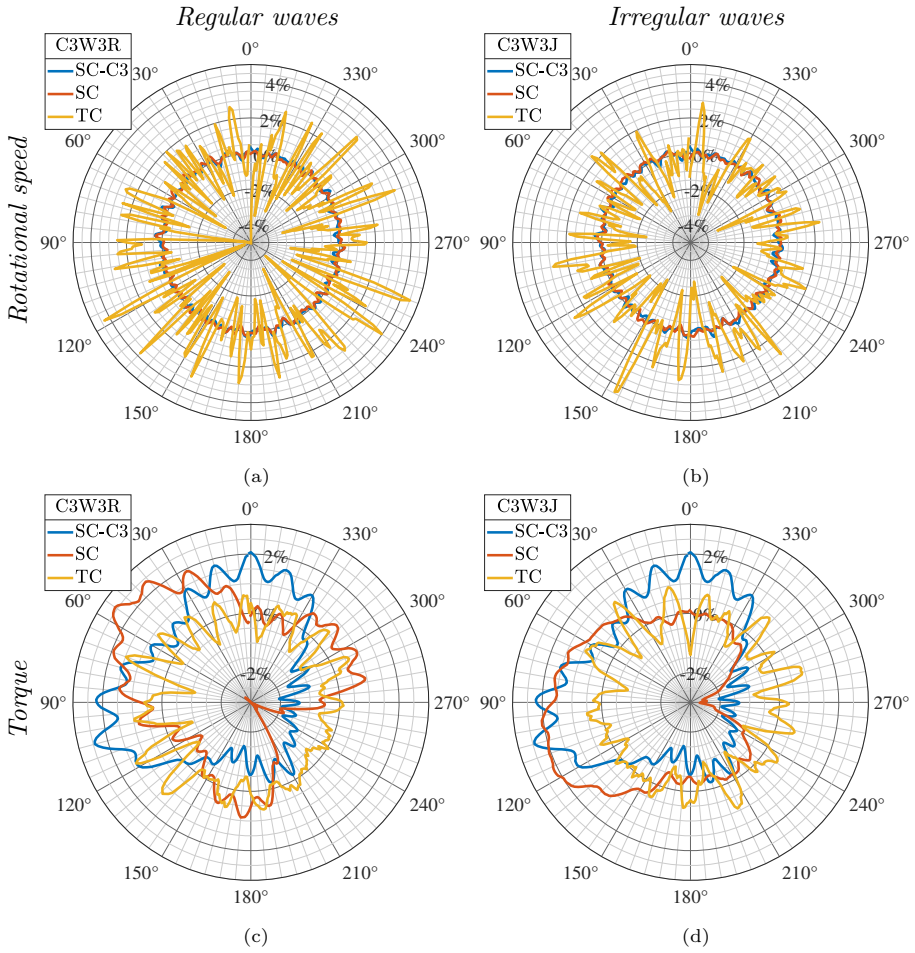

Figure 15: Front view of the rotor with angle-averaged rotational speed (top figures) and torque (bottom figures) in speed and torque control for $TSR = 7$. Plotted as a percentage of the mean values. (a,c) regular waves (C3W3R), (b,d) irregular waves (C3W3J). Current-only case SC-C3 added for comparison.

In Figure 16 the thrust (a) and torque (b) data are angle-averaged for two cases: current-only and combined waves and current in speed and torque control. From these results, it is clear that the thrust behaved in a similar manner for the speed control cases. For the torque control case, thrust fluctuations stay close to 0% during a full revolution. The torque data presents the three-lobed shape in the speed control case but not for the current-only and torque control cases. In both sub-figures the data present the notch at around 240°.

Although the variation ranges were small (±3%) the thrust fluctuations in the presence of waves were 2-3 times higher than the ones under current only.

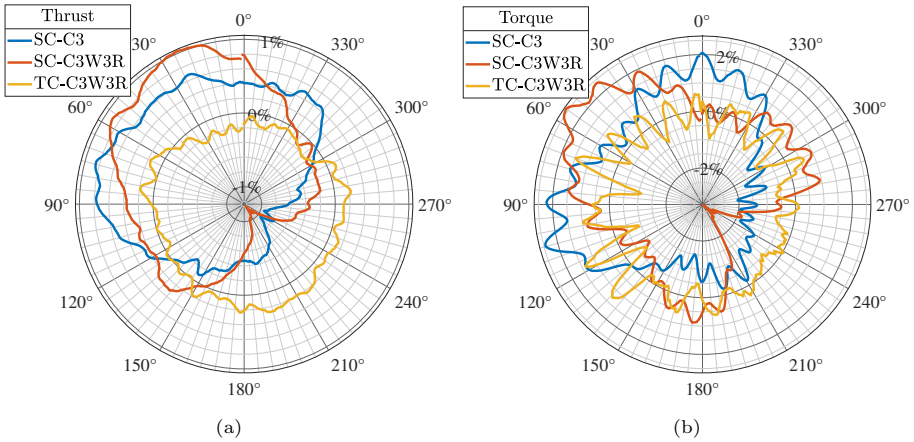

Figure 16: Angle averaged a) thrust and b) torque for current-only case SC-C3, wave case C3W3R in speed and torque control at $TSR = 7$

4.3. Loading fluctuations

Following analysis from [17] and [39], the loading fluctuations in the time domain are analysed in this section. From Sections 4.1 and 4.2, it was observed that the average turbine loading were insignificantly influenced by the addition of waves or the control strategy selected.

Fluctuating loads have an impact in power control, grid integration and structural and mechanical design of the different components that comprise a turbine. This analysis looked into the frequency and amplitude of these fluctuations.

In Figures 17, 18 and 19 the variation with TSR of the average loading ranges (a) and average maximum and minimum values (b) of the rotational speed, torque and thrust, respectively, are presented for all tests.

The range of the rotational speed as a function of the average rotational speed is shown in Figure 17a for all cases. In the torque control cases, the relative rotational speed fluctuations decreased as the TSR increased, but both maximum and minimum RPM values increased as TSR increased (Figure 17b). The range of fluctuation of the rotational speed under speed control was kept well below 10% for the regular wave cases. For the current-only cases it decreased steadily from a maximum of 6% to a minimum of 1% as TSR increased7. For the torque control cases the rotational speed range went up to around 70% of the average rotational speed for regular waves and 30% for irregular waves. Similar findings were reported in [18].

The range between maximum and minimum values was of around 80 RPM for the torque control cases and around 4 RPM for the speed control cases. Under torque control, the irregular wave cases showed a range half of the regular wave cases.

In Figure 18 the fluctuations in the torque signals are presented. For the current-only cases the torque range seems to decrease for $TSR < 3$ and increase up to 45% for $TSR > 3$. For the speed control cases, there is an increase in the torque fluctuation range with increasing TSR (Figure 18a). At $TSR = 7$ there is a fluctuation range of 100% of the mean torque value for the highest waves (C3W3R), 55% for the irregular waves (C3W3J) and 45% for the current-only case (C3). Similar behaviours between regular and irregular waves were found in [17, 18]. There is a clear correlation between wave height and fluctuations range. As wave height increases, the fluctuation range increases. In torque control, for both regular and irregular waves, the torque range went up to around 60% from the mean torque values at the higher TSR. Comparing control strategies, the difference between speed and torque control for case C3W3R goes up to 55% at $TSR = 5$. In Figure 18b, the average torque range under speed control was around 20 Nm and 5 Nm for the torque control cases. Although the range

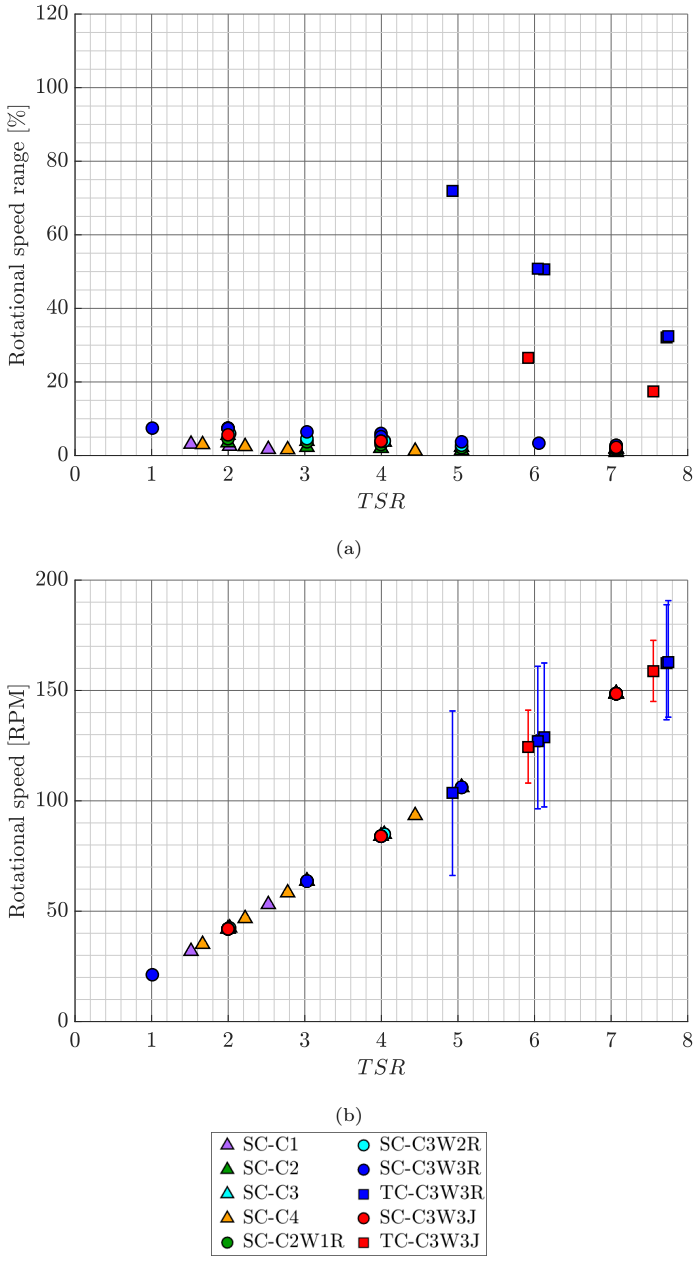

Figure 17: Average rotational speed fluctuation per wave period (speed and torque control cases) a) fluctuation range as a function of the average rotational speed. b) average rotational speed values with error bars representing maximum and minimum values.

increases as TSR increases in Figure 18a, the maximum and minimum values decrease as TSR increases in Figure 18b.

Figure 19 shows the thrust fluctuations for all the tests. Similar to torque (Figure 18a), for the current-only cases, thrust range decreases for $TSR < 3$ and increases for $TSR > 3$. For the torque control cases, relative thrust range decreases as TSR increases The cases with the largest wave (C3W3R) have the strongest influence in the thrust fluctuations. In torque control, the range observed (Figure 19a) is 75% of the average thrust. In contrast, under speed control this range is only 40%. At approximately $TSR \approx 7$ the ranges of torque and speed control of wave C3W3R appeared to match. From the slopes, it is anticipated that for $TSR > 7$, the thrust fluctuations for speed control could be higher than for torque control. It is unknown how high and low these values could reach. At around $TSR = 5$ the thrust range for the torque control cases was found to be 35% higher than the speed control case. At $TSR \approx 3$ (max C_P), a thrust range of 35% is observed for the highest waves. In contrast, [18] reported a higher thrust range of 50% with the same turbine but with different pitch angles at a towing tank. Similarly, [16] reported a range of 65% at $TSR \approx 7$ (max C_P) with a different turbine at FloWave. This differences in the thrust range could be due to the different flow characteristics linked to each facility but also to the different turbine models.

For regular waves cases, recirculating tank testing shows twice the rotational speed and thrust ranges than the towing tank testing under torque control [18]. This difference could be associated to the turbulent nature of the flow in the recirculating tank. It was not possible to make a full comparison of the torque control tests as the TSR values used in each of the studies did not fully overlap due to the turbulence-induced stall.

For irregular waves cases, the quantified parameters show fluctuation ranges values similar (within 10%) between recirculating tank data and towing tank data. However, the recording time at the towing was was half of the duration at the recirculating tank. Towing tank results may have presented wave reflection effects.

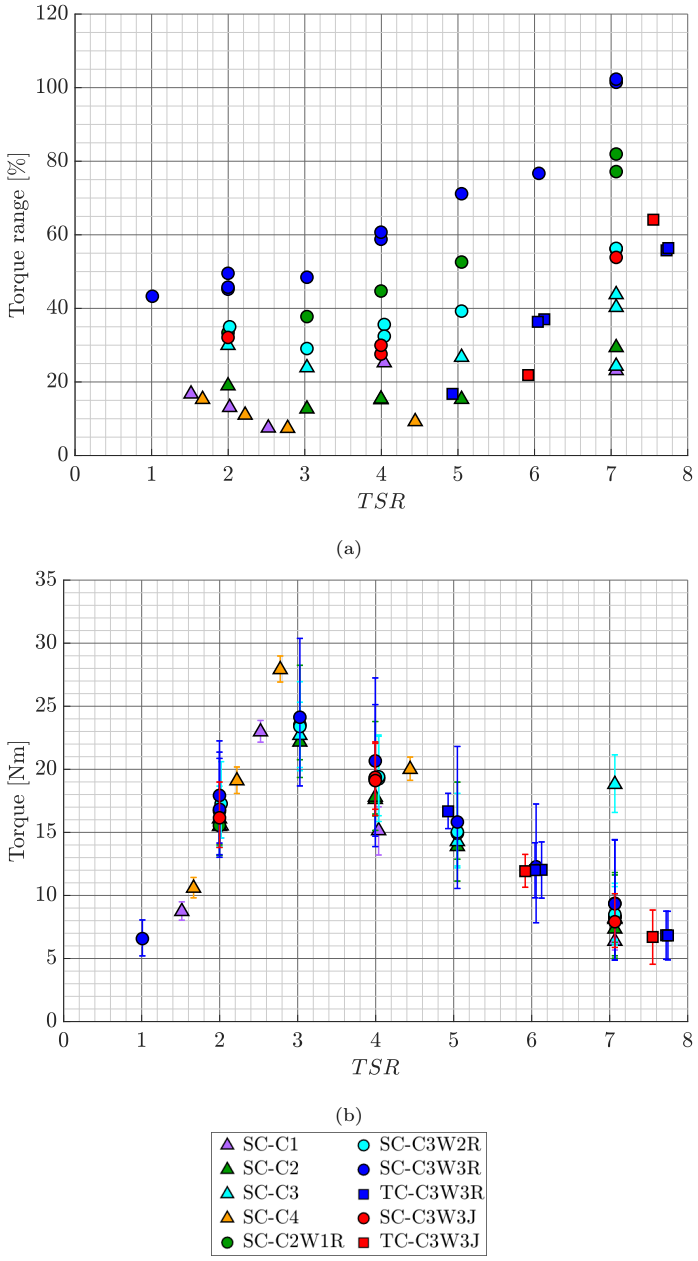

Figure 18: Average torque fluctuation per wave period (speed and torque control cases) a) fluctuation range as a function of the average torque. b) average torque values with error bars representing maximum and minimum values.

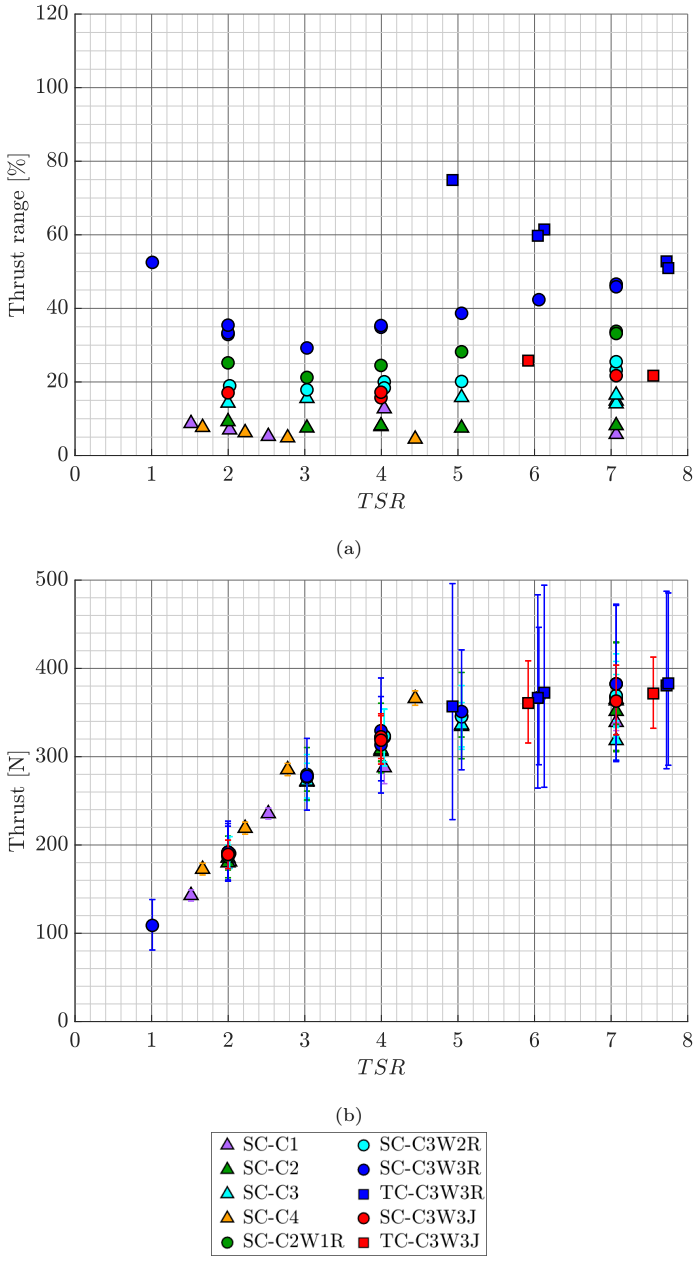

Figure 19: Average thrust fluctuation per wave period (speed and torque control cases) a) fluctuation range as a function of the average thrust. b) average thrust values with error bars representing maximum and minimum values.

Figure 20 shows the RBM fluctuations and range of blade 3 in similar fashion to Figures 17-19. Comparing the RBM fluctuations (Figures 20a) with the thrust fluctuations from Figure 19a, it is possible to see the close resemblance in behaviour. Case SC-C3W3R is the one with strongest disagreement between RBM and thrust. For the thrust, the data has a smooth concave shape whereas for the RBM the data is flatter with gaps between repeat values at $TSR = 2$ and 4. This difference is yet to be understood. The main difference between RBM and thrust values in Figures 20b and 19b is the operational range. SD values behave similarly for both signals. Under speed control, SC increases as TSR increases and decreases as TSR increases under torque control.

The relation between average wave height and average thrust range is explored in Figure 21. It is clear that the average thrust range increased with the average wave height. Under torque control, the thrust range fell further away from the average thrust than the homologous speed control cases. This difference between control strategies is still an unknown. The vertical scatter seen at each average wave height is related to the TSR of each run as seen on Figure 19a. Meaning that the influence of the rotational speed on the thrust fluctuations was higher than the influence of the wave height.

4.4. Phasing of loading patterns

Similar to the procedure described in [39], the relation between periodic signals or here referred as "phase difference" is analysed in this section. The phase difference between the thrust and the water surface elevation is plotted in Figure 22 for the wave case C3W3R at all $TSRs$. Using zero-up and zero-down methods, it can be seen that regardless of the method used, the phase difference observed was positive with a mean phase difference of about 20°. This positive phase difference means that the thrust was being sensed by the rotor before the wave had reached the rotor plane.

The phase difference between thrust and water surface elevation for case C3W3R under speed and torque control is plotted against TSR in Figure 23. The high standard deviation values indicated by the error bars agree with the

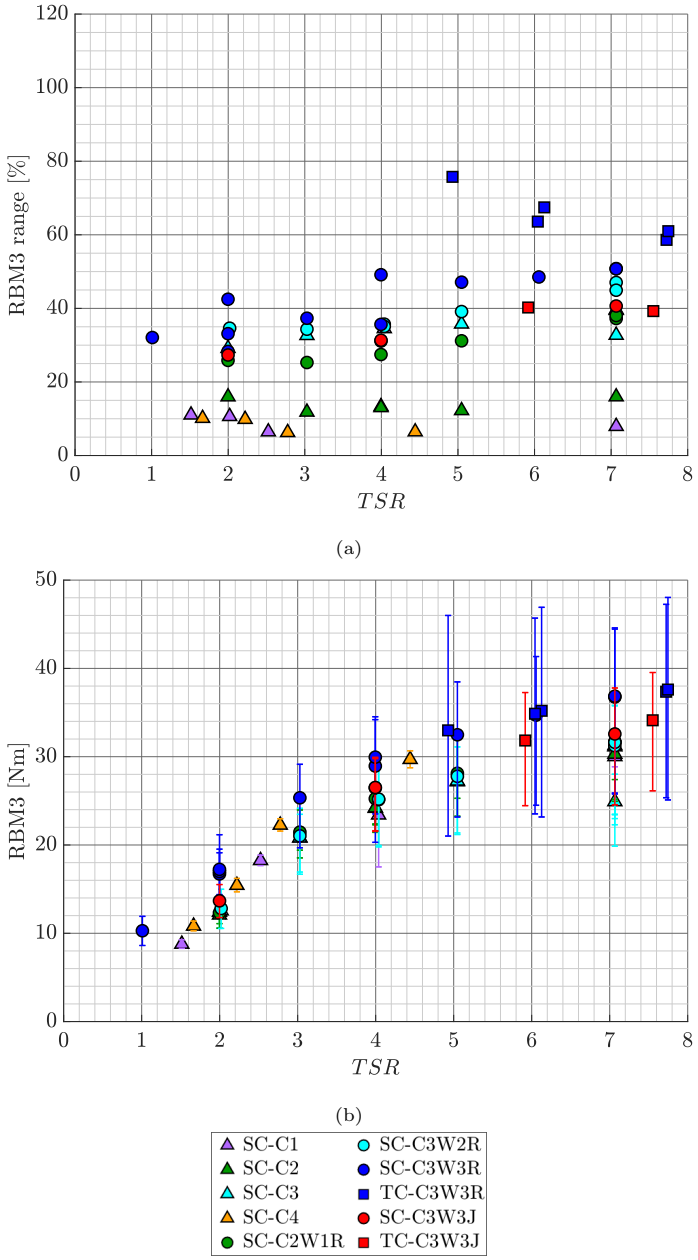

Figure 20: Average RBM fluctuation per wave period for blade 3 (speed and torque control cases) a) fluctuation range as a function of the average RBM of blade 3. b) average RBM values with error bars representing maximum and minimum values.

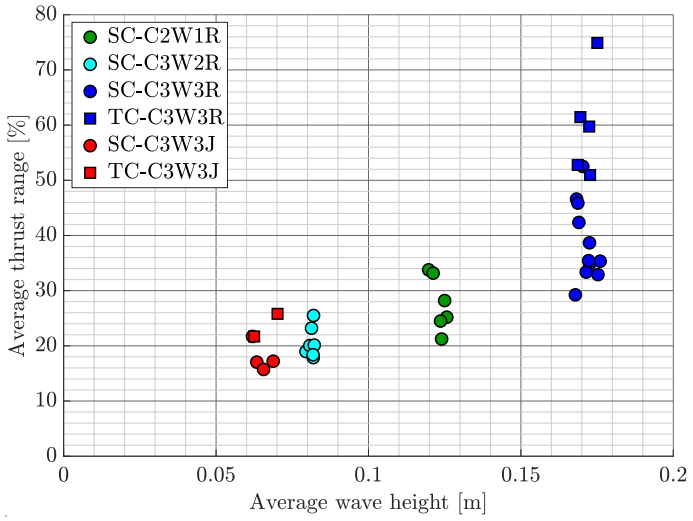

Figure 21: Average thrust range as a function of average wave height for all wave cases.

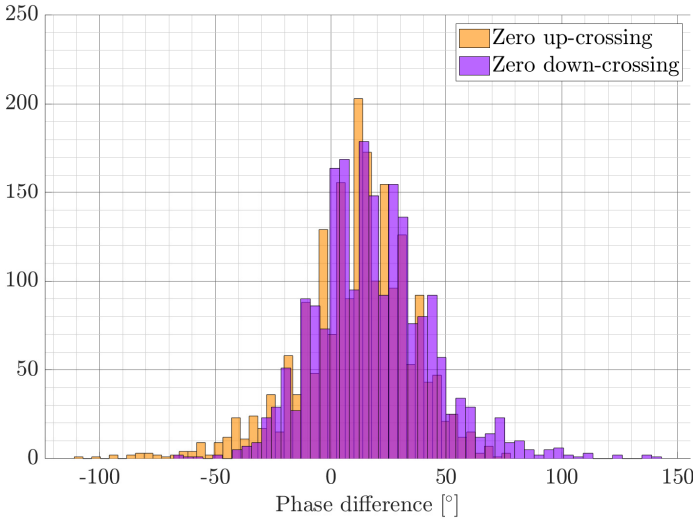

Figure 22: Zero up-crossing and zero down-crossing histograms of phase difference between rotor thrust and water surface elevation signals for all regular wave cases.

spread shown in the histogram of Figure 22. For the speed control case, the phase difference has a concave shape, with the highest value of 30° at $TSR = 2$. Phase difference values decrease with TSR down to 10° at $TSR \approx 4$. For $TSR > 4$, the phase difference slowly increases with TSR up to 15° at $TSR > 6$. There is a ∼5° phase difference between control strategies.

The phase difference shown in Figure 23 means that each peak in the thrust signal occurred between approximately 5° and 30° before the peak in the surface elevation signal. This difference represents a significant lag between the two measurements.

These results fall short from the average values presented in [17], where they reach an 80° lag between the surface elevation and the thrust signals under speed control and 65° under torque control. This differences could be attributed to the fact that the waves generated in the recirculating tank show more variability but are also influenced by wave-current interaction effects.

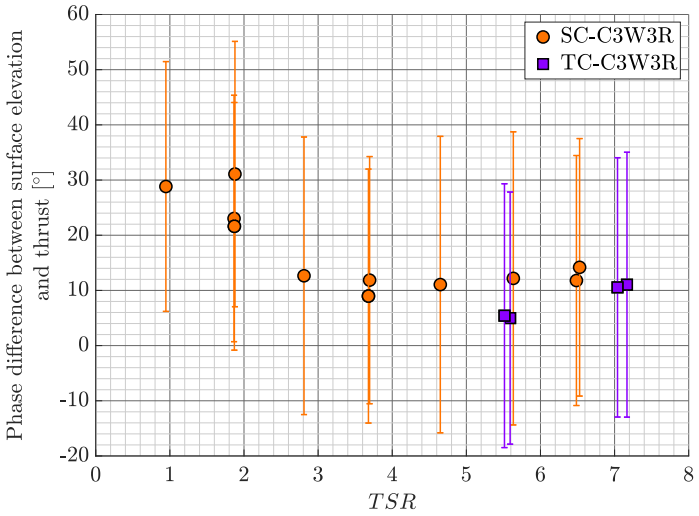

Figure 23: Phase difference between surface elevation and thrust for different TSR values with error bars. For same wave in different control mode: SC-C3W3R and TC-C3W3R.

The random nature in the wave period of the irregular wave cases did not allow for phase averaging as with the regular wave cases. In Figure 24, the

phase difference in the signals is investigated by plotting the time series of the signals side by side. To facilitate comparison of the time series the signals have been re-scaled.

Similar to findings in [39], it is not possible to see any evident phasing between the water surface elevation with irregular waves and thrust signals as in [17]. One possible explanation is that the velocity depth profiles and turbulence intensity of the flume tank masked the phasing feature in comparison to the more uniform flow in the towing tank tests from [17].

Comparing control strategies, it is possible to see a difference with the controlled signal. Under torque control, the torque signal seems to be out of phase of the wave height signals by around 180°. Similar behaviour is seen for the rotational speed signal under speed control. In both cases, the uncontrolled parameters follow the water surface elevation signal. When the surface elevation is at a crest, the wave particle velocity is at its highest and therefore, the control system has to actively change the values of the controlled parameter to keep the turbine running the same way (i.e. the uncontrolled parameters following the water surface elevation signal).

In Figure 25 a comparison between TSR values for the case SC-C3W3J is shown. At $TSR = 2$, the turbine operates in its stall region and it is possible to see how the signals behave differently that at $TSR = 7$. In the stall region, the torque signal shows a phase difference from the water surface elevation but also its shape is closer to the rotational speed signal shape than to the thrust's as it is perceived at $TSR > 3$. At $TSR > 3$, when the rotational speed is controlled to keep it constant as the wave orbital changes.

Looking into the phasing between the instantaneous power and the wave height and flow velocity, it is clear that both have an effect on the power generated. Figure 26 shows how the power follows the flow velocity changes in time and at the same time the fluctuating nature of the waves is also noticeable in the instantaneous power.

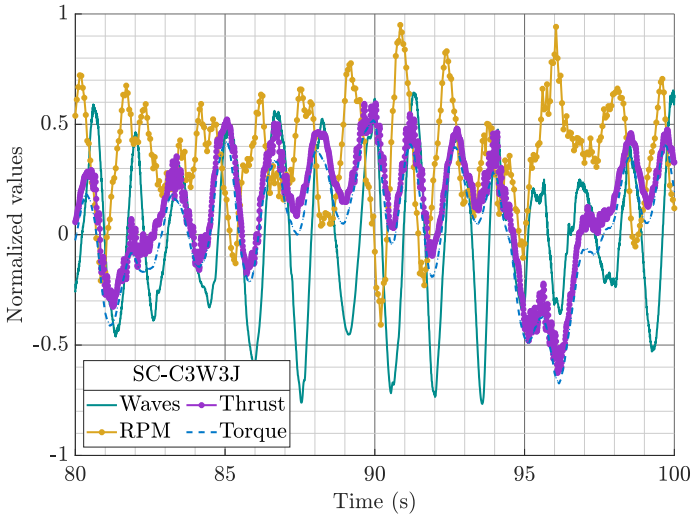

(a)

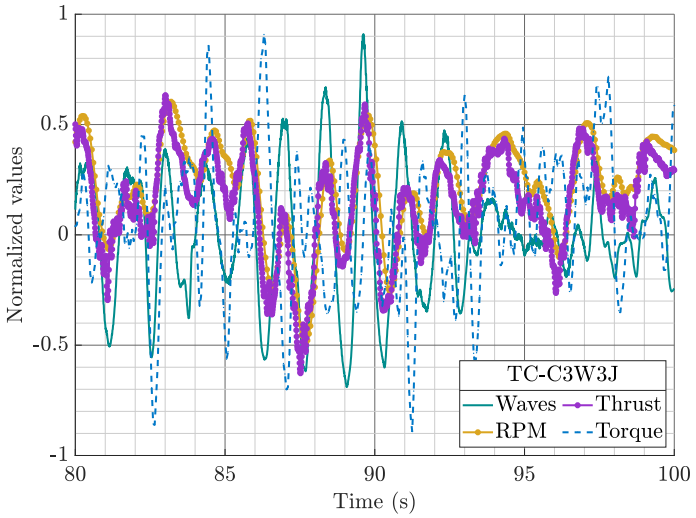

(b)

Figure 24: Comparison of water surface elevation, rotational velocity, rotor thrust and torque signals in irregular waves under a) speed control b) torque control. $TSR = 7$

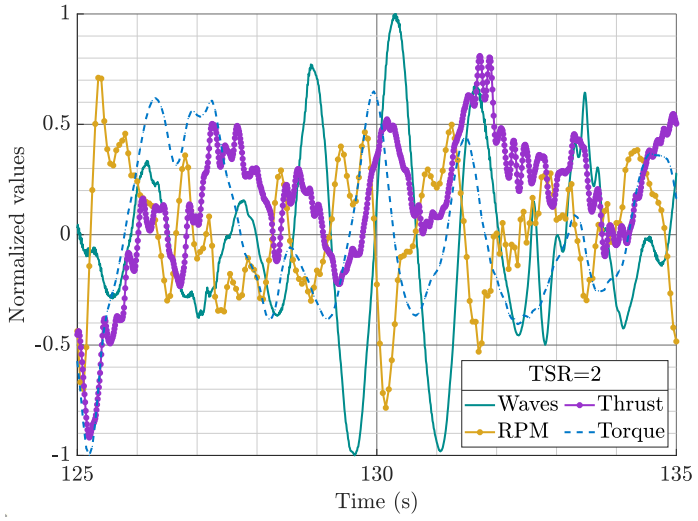

(a)

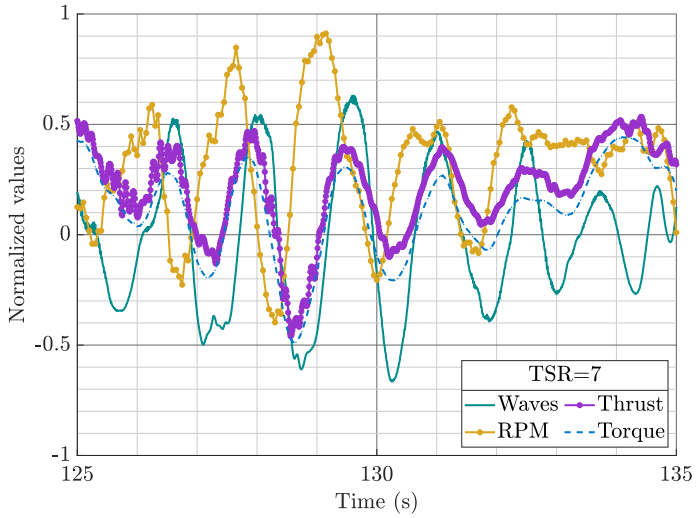

(b)

Figure 25: Comparison of water surface elevation, rotational velocity, rotor thrust and torque signals in irregular waves at a) $TSR = 2$ b) $TSR = 7$.

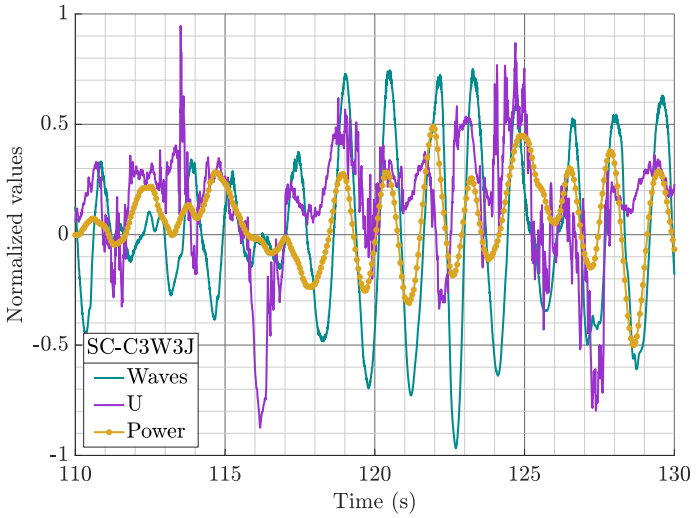

(a)

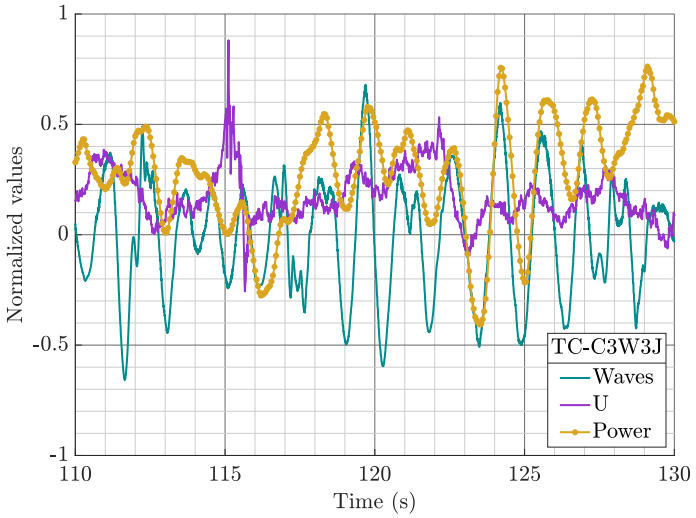

(b)

Figure 26: Comparison of water surface elevation, flow velocity signals and instantaneous power in irregular waves under a) speed control b) torque control

4.5. Frequency domain analysis

A Fast Fourier Transform (FFT) was undertaken to analyse the fluctuation of the turbine loads in the frequency domain. Figure 27 groups the thrust spectra of all the wave cases under speed control at $TSR = 4$. The frequency (horizontal) axis is normalised by the rotational frequency. Apart from the SC-C2W1R case, the rest of the cases follow a very similar trend staying close to each other. This difference appears to be linked to the difference in the turbulence and velocity depth profiles associated to the presence of the wave makers presented in Section 3. The first large peak in each curve is the one associated to the wave frequency. The difference between wave frequencies is noticeable, especially for the irregular waves, where the peak is wider, with less amplitude and not as defined as the regular wave cases. The peak at $1f/f_0$ is the one associated to the rotational frequency of the rotor that happens once per revolution and the peak at $3f/f_0$ is the one associated to the three rotor blades. From these results, it can be deduced that regardless of the incoming waves, the thrust loading behaved in similar manner.

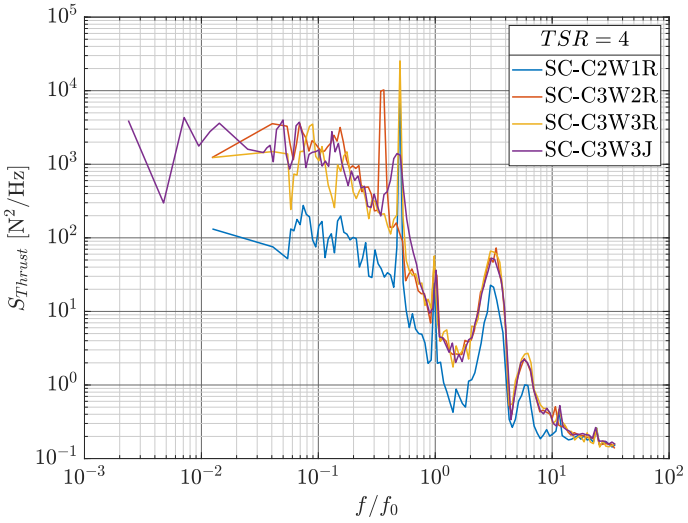

Figure 27: Thrust signal in the frequency domain for all wave cases on speed control at $TSR = 4$.

Figure 28 looks at the influence of TSR on the thrust spectra for case SC-C3W3R. In Figure 28a, the thrust spectra are plotted against frequency. In this case the first peak on each signal matches in all the TSR signals. The different peaks on the right hand side of these peaks associated to the wave frequency represent the rotational frequency and the blades passage frequency. These peaks are easier to identify on Figure 28b, where the frequency is normalised by the rotational frequency of the rotor. It is possible to see how the rotational frequency was half the wave frequency at $TSR = 1$. At $TSR = 2$ wave and rotational frequencies shared the same value and at $TSR = 4$ the rotational frequency was double the wave frequency. It is worth noting that having the same frequency of rotational velocity as the wave frequency does not lead to the amplification of the wave induced thrust load oscillation. In all cases, the blades passage frequency at $3f/f_0$ was present.

Now, the difference between control modes and wave type is explored. Figure 29 shows the power spectra in speed (purple) and torque (orange) control modes for regular waves (solid) and irregular waves (dashed). Overall, all of the cases show a similar behaviour. The torque control cases have a lower energy content than the speed control cases of about one order of magnitude. The main difference is that the peaks associated to the rotational frequency and blades passage ($f/f_0 = 1$ and $f/f_0 = 3$) were visible for the torque control cases. The lack of presence of these fluctuations in the power under torque control indicate that the power generation is not affected by the mechanical artefacts associated to the turbine's rotation.

Figure 30 explores how the control mode influences the controlled parameter and how the parameter that is not controlled behaves. Figure 30a is for regular waves (C3W3R). The frequency axis is normalised by the rotational frequency. In this case, torque signals (solid lines) behaved very differently depending on the control mode. In torque control, the frequency response was almost flat. The gap between the torque control signals is about three orders of magnitude at lower frequencies. This behaviour repeated for the rotational speed cases but in this case, the flat signal is the one under speed control. This means that the

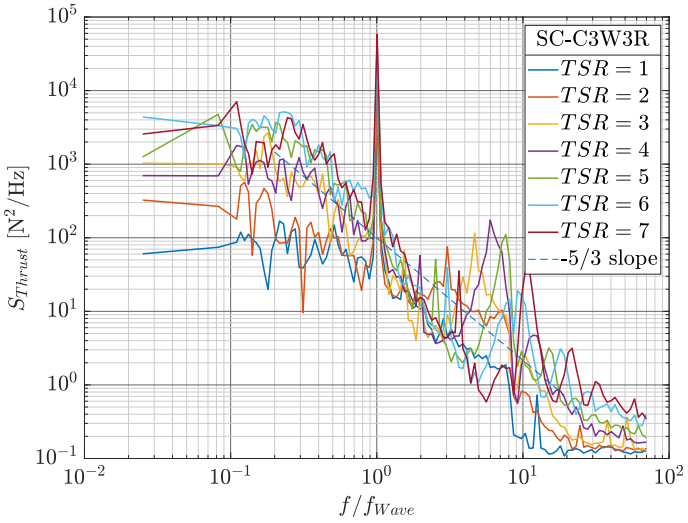

(a)

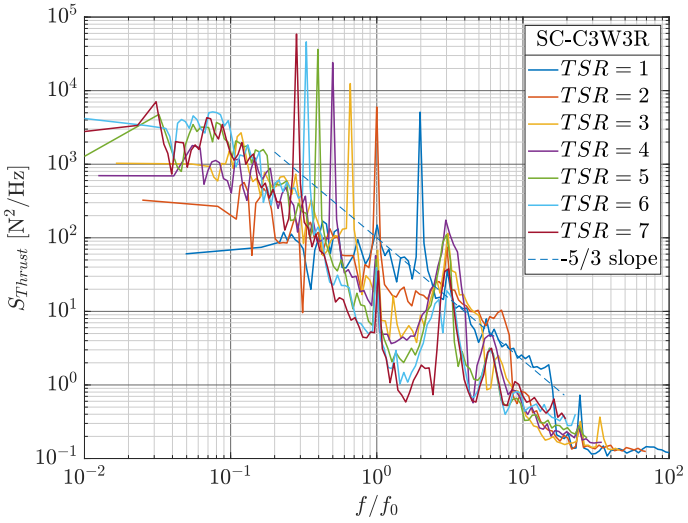

(b)

Figure 28: Thrust signal in the frequency domain for case SC-C3W3R. U=1 m/s; H=0.19 m; F=0.7 Hz. a) frequency normalised by the wave frequency, b) frequency normalised by the rotational speed

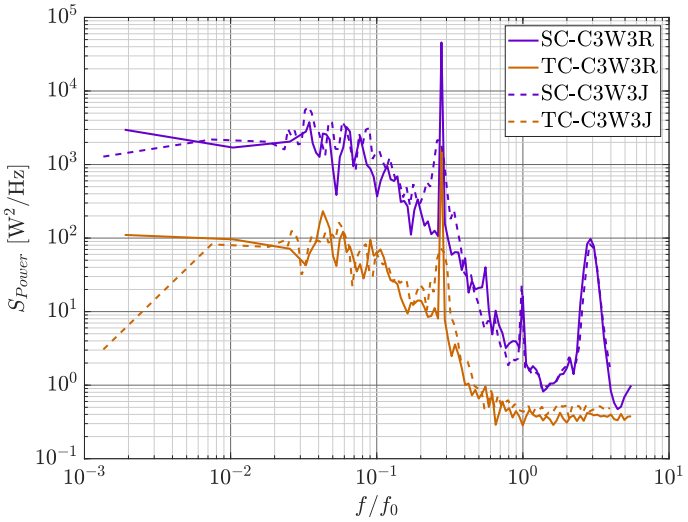

Figure 29: Power signal in the frequency domain for cases SC-C3W3R, TC-C3W3R, SC-C3W3J, TC-C3W3J. $TSR \approx 7$.

parameter that is under control had very little frequency response compared to the uncontrolled parameter. The irregular wave case (C3W3J) on Figure 30b followed the same trend as in Figure 30a. The main difference is the definition of the peaks. An interesting artefact to consider is how flat the torque spectra under torque control is. Neither the peaks associated to the waves nor the peaks associated to the rotation of the turbine are present. Unlike with the rotational speed spectra under speed control that all these peaks are very visible. This artefact was also observed in [18].

5. Conclusions

This work reports on an experimental campaign on a three bladed horizontal axis tidal turbine performed at the recirculating wave flume located at the French institute IFREMER. The model was subjected to current-only and combined regular and irregular wave and current conditions. The highest wave case (W3R) and the irregular wave case (W3J) were tested in speed and torque control. The rest of the flow conditions were tested under speed control only.

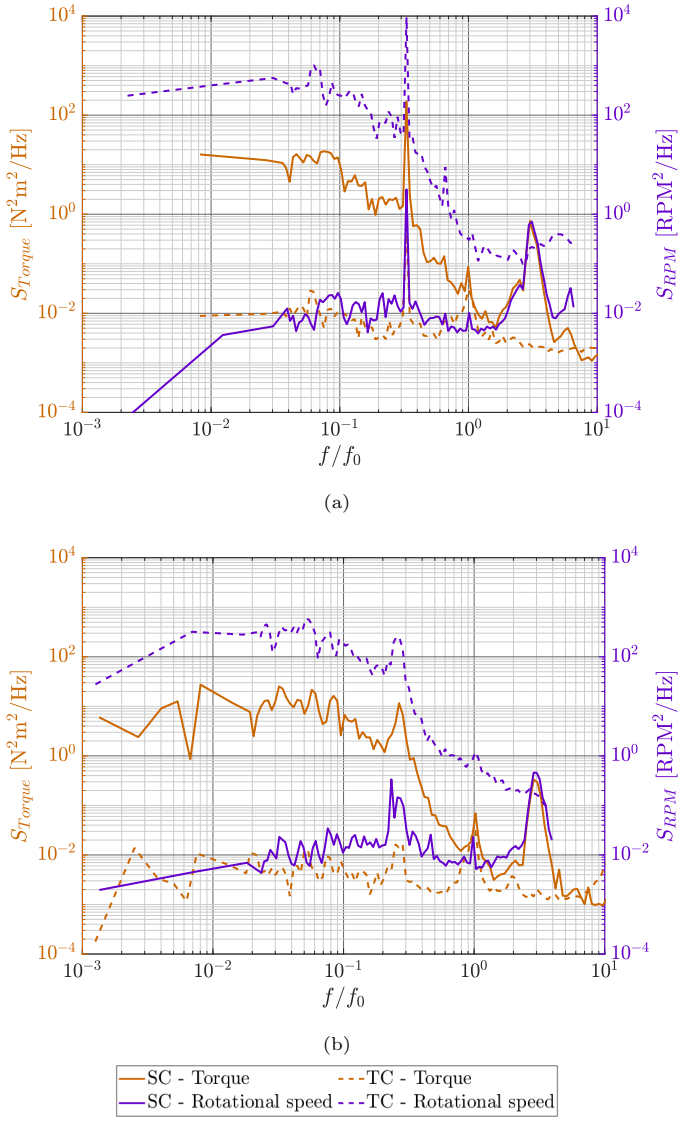

Figure 30: Torque and rotational speed in the frequency domain. $TSR \approx 7$. a) regular wave case C3W3R in speed and torque control, b) irregular wave case C3W3J in speed and torque control.

Rotor thrust and torque and blade root bending moment were recorded along with flow velocity and wave height. The main conclusions from the study are:

1. Under torque control, the average thrust range was around 75% higher than the mean value.
2. Applying a constant torque significantly increased the thrust fluctuations. There was a 35% increase in the fluctuations magnitude compared to constant speed tests.
3. The rotational speed signal under speed control and torque signal under torque control have standard deviation values below 10% of the average values.
4. The rotational speed signal under torque control and torque signal under speed control have standard deviation values up to 25% and 50% of the average values, respectively.
5. The addition of waves and the control strategy have an impact of 5% on the average loads from the current-only cases.
6. Beside the wave-induced and turbulence-induced loading, the rotor also experiences three fluctuations each revolution associated to the blades passing in front of the stanchion. These fluctuations are characterised by a three lobed shape with each lobe 120° apart from each other.
7. Each blade experienced a dip in the RBM signal when passing in front of the stanchion.
8. Fluctuations ranges are two times higher for regular waves under torque control than for towing tank tests. For irregular waves, values are within 10%.
9. The influence of the rotational speed on the thrust fluctuations was higher than the wave height changes.
10. Turbine loading had a positive phase difference with the water surface elevation, meaning that the turbine sensed the waves before they reached the rotor plane. Around the optimum TSR, the phase difference was the lowest.

11. Phase difference for torque control was about 5° smaller than for speed control.
12. When comparing control strategies in the frequency domain, the controlled parameters contained three times less energy than the uncontrolled parameters at the lower frequencies.

Future work includes the use of blockage correction factors to allow direct comparison between the different testing campaigns that are part of the project. Longer testing time for irregular waves would allow for better convergence so the criteria $H = H_S$ is met. Further testing would allow an extended test plan to include repeats of tests already conducted, the study of other control strategies in the performance of turbines and array testing. These results will serve to validate the numerical models developed as part of the DyLoTTA project as well as providing new insights and confirming previous knowledge into wave-current loading on tidal turbines.

6. Acknowledgements

This laboratory study was funded by the Engineering and Physical Sciences Research Council (EPSRC) under the Cardiff University Impact Acceleration Account [EP/R51150X/1] and the Dynamic Loadings on Turbines in a Tidal Array (DyLoTTA) project [EP/N020782/1]. The authors would like to thank the staff at IFREMER for their expertise and support during testing.

References

[1] A. S. Bahaj, A. F. Molland, J. R. Chaplin, W. M. J. Batten, Power and thrust measurements of marine current turbines under various hydrodynamic flow conditions in a cavitation tunnel and a towing tank, Renewable Energy 32 (3) (2007) 407–426. doi:10.1016/j.renene.2006.01.012.

[2] B. Morandi, F. Di Felice, M. Costanzo, G. P. Romano, D. Dhomé, J.-C. Allo, Experimental investigation of the near wake of a horizontal axis tidal

current turbine, International Journal of Marine Energy 14 (2016) 229–247. doi:10.1016/j.ijome.2016.02.004.

[3] D. A. Doman, R. E. Murray, M. J. Pegg, K. Gracie, C. M. Johnstone, T. M. Nevalainen, Tow-tank testing of a 1/20th scale horizontal axis tidal turbine with uncertainty analysis, International Journal of Marine Energy 11 (2015) 105–119. doi:10.1016/j.ijome.2015.06.003.

[4] B. Gaurier, G. Germain, J.-V. Facq, C. M. Johnstone, A. D. Grant, A. H. Day, E. Nixon, F. Di Felice, M. Costanzo, Tidal energy "Round Robin" tests. Comparisons between towing tank and circulating tank results, International Journal of Marine Energy 12 (December) (2015) 87–109. doi:10.1016/j.ijome.2015.05.005.

[5] B. Gaurier, P. Davies, A. Deuff, G. Germain, Flume tank characterization of marine current turbine blade behaviour under current and wave loading, Renewable Energy 59 (2013) 1–12. doi:10.1016/j.renene.2013.02.026.

[6] N. Barltrop, K. S. Varyani, A. D. Grant, D. Clelland, X. P. Pham, Investigation into wave—current interactions in marine current turbines, Proceedings of the Institution of Mechanical Engineers, Part A: Journal of Power and Energy 221 (2) (2007) 233–242. doi:10.1243/09576509JPE315.

[7] T. A. de Jesus Henriques, S. C. Tedds, A. Botsari, G. Najafian, T. S. Hedges, C. J. Sutcliffe, I. Owen, R. J. Poole, The effects of wave-current interaction on the performance of a model horizontal axis tidal turbine, International Journal of Marine Energy 8 (December 2014) (2014) 17–35. doi:10.1016/j.ijome.2014.10.002.

[8] P. W. Galloway, L. E. Myers, A. S. Bahaj, Studies of a scale tidal turbine in close proximity to waves, in: Proceedings of the 3rd International Conference on Ocean Energy, Bilbao, Spain, 2010, pp. 1–6.

[9] S. Ordonez-Sanchez, K. Porter, C. H. Frost, M. Allmark, C. M. Johnstone, T. O'Doherty, Effects of Wave-Current interactions on the performance of

tidal stream turbines, in: Proceedings of the 3rd Asian Wave and Tidal Energy Conference, Singapore, Singapore, 2016, pp. 978–981. doi:10.3850/978-981-11-0782-5.

[10] R. Martinez, G. S. Payne, T. Bruce, The effects of oblique waves and current on the loadings and performance of tidal turbines, Ocean Engineering.

[11] S. Draycott, A. Nambiar, B. G. Sellar, T. A. D. Davey, V. Venugopal, Assessing extreme loads on a tidal turbine using focused wave groups in energetic currents, Renewable Energy 135 (2019) 1013–1024. doi:10.1016/j.renene.2018.12.075.

[12] S. Draycott, G. S. Payne, J. Steynor, A. Nambiar, B. G. Sellar, V. Venugopal, An experimental investigation into non-linear wave loading on horizontal axis tidal turbines, Journal of Fluids and Structures 84 (2019) 199–217. doi:10.1016/j.jfluidstructs.2018.11.004.

[13] T. M. Nevalainen, The effect of unsteady sea conditions on tidal strea mturbine loads and durability, Ph.D. thesis, Strathclyde University (2016).

[14] H. R. Mullings, T. J. Stallard, G. S. Payne, Operational Loads On A Tidal Turbine due to Environmental Conditions, in: Proceedings of the International Offshore and Polar Engineering Conference, Vol. June 25-30, San Francisco, 2017, pp. 1–8.

[15] M. J. Lewis, J. McNaughton, C. Márquez-Dominguez, G. Todeschini, M. Togneri, I. Masters, M. Allmark, T. Stallard, S. Neill, A. Goward-Brown, P. Robins, Power variability of tidal-stream energy and implications for electricity supply, Energydoi:10.1016/j.energy.2019.06.181.

[16] S. Draycott, J. Steynor, A. Nambiar, B. Sellar, V. Venugopal, Experimental assessment of tidal turbine loading from irregular waves over a tidal cycle, Journal of Ocean Engineering and Marine Energy 5 (2) (2019) 173–187. doi:10.1007/s40722-019-00136-9.

[17] K. Porter, S. Ordonez-sanchez, M. Allmark, R. Ellis, C. Lloyd, O. Doherty, C. Johnstone, Laboratory Study of Tidal Turbine Performance in Irregular Waves, in: Proceedings of the 4th Asian Wave and Tidal Energy Conference, Taipei, Taiwan, 2018, pp. 1–9.

[18] S. Ordonez-Sanchez, M. Allmark, K. Porter, R. Ellis, C. Lloyd, I. Santic, T. O'Doherty, C. Johnstone, Analysis of a Horizontal-Axis Tidal Turbine Performance in the Presence of Regular and Irregular Waves Using Two Control Strategies, Energies 12 (3) (2019) 367. doi:10.3390/en12030367.

[19] M. J. Harrold, Experimental and numerical assessment of a tidal turbine control strategy, Ph.D. thesis, University of Strathclyde (2016).
URL http://ethos.bl.uk/OrderDetails.do?uin=uk.bl.ethos.723008

[20] M. Arnold, F. Biskup, P. W. Cheng, Load Reduction Potential of Variable Speed Control Approaches for Fixed Pitch Tidal Current Turbines, in: Proceedings of the 11th European Wave and Tidal Energy Conference, Elsevier Ltd, 2015, pp. 1–10. doi:10.1016/j.ijome.2016.04.012.
URL http://dx.doi.org/10.1016/j.ijome.2016.04.012

[21] A. Olczak, The Influence of Waves on Tidal Stream Turbine Arrays, Ph.D. thesis, The University of Manchester (2015).

[22] X. Yin, W. Zhang, Z. Jiang, L. Pan, M. Lei, Adaptive backstepping control for maximizing marine current power generation based on uncertainty and disturbance estimation, International Journal of Electrical Power & Energy Systems 117 (2020) 105329. doi:https://doi.org/10.1016/j.ijepes.2019.05.066.
URL http://www.sciencedirect.com/science/article/pii/S0142061518327996

[23] X. Yin, X. Zhao, ADV Preview Based Nonlinear Predictive Control for Maximizing Power Generation of a Tidal Turbine with Hydrostatic Transmission, IEEE Transactions on Energy Conversion 34 (4) (2019) 1781–1791. doi:10.1109/TEC.2019.2938062.

[24] B. Gaurier, G. Germain, J.-V. Facq, B. Thomas, Wave and current flume tank of IFREMER at Boulogne-sur-mer. Description of the facility and its equipment, Tech. rep., Institut Français de Recherche pour l'Exploitation de la Mer (IFREMER) (2018). doi:10.13155/58163.

[25] M. Allmark, R. Ellis, K. Porter, T. O. Doherty, C. Johnstone, The Development and Testing of a Lab-Scale Tidal Stream Turbine for the Study of Dynamic Device Loading, in: Proceedings of the 4th Asian Wave and Tidal Energy Conference, Taipei, Taiwan, 2018, pp. 1–10.

[26] M. Allmark, Condition monitoring and fault diagnosis of tidal stream turbines subjected to rotor imbalance faults, Ph.D. thesis, Cardiff University (2016).
URL http://orca.cf.ac.uk/98633/

[27] A. Mason-Jones, Performance assessment of a horizontal axis tidal turbine in a high velocity shear environment, Ph.D. thesis, Cardiff University (2010).

[28] R. Ellis, M. Allmark, T. O. Doherty, A. Mason-jones, S. Ordonez-sanchez, K. Johannesen, C. Johnstone, Design Process for a Scale Horizontal Axis Tidal Turbine Blade ., in: Proceedings of the 4th Asian Wave and Tidal Energy Conference, Taipei, Taiwan, 2018, pp. 1–8.

[29] A. Mason-Jones, D. O'Doherty, C. Morris, T. O'Doherty, C. Byrne, P. Prickett, R. Grosvenor, I. Owen, S. Tedds, R. Poole, Non-dimensional scaling of tidal stream turbines, Energy 44 (1) (2012) 820 – 829, integration and Energy System Engineering, European Symposium on Computer-Aided Process Engineering 2011. doi:https://doi.org/10.1016/j.energy.2012.05.010.
URL http://www.sciencedirect.com/science/article/pii/S0360544212003891

[30] B. Gaurier, G. Germain, G. Pinon, How to correctly measure turbulent upstream flow for marine current turbine performances evaluation?, in:

Advances in Renewable Energies Offshore: Proceedings of the 3rd International Conference on Renewable Energies Offshore, Lisbon, 2018, pp. 23–30.

[31] W. M. J. Batten, A. S. Bahaj, A. F. Molland, J. R. Chaplin, The prediction of the hydrodynamic performance of marine current turbines, Renewable Energy 33 (5) (2008) 1085–1096. doi:10.1016/j.renene.2007.05.043.

[32] I. G. Bryden, S. J. Couch, A. Owen, G. Melville, Tidal current resource assessment, Proceedings of the Institution of Mechanical Engineers, Part A: Journal of Power and Energy 221 (2) (2007) 125–135. doi:10.1243/09576509JPE238.

[33] S. Serhadlıoğlu, T. A. Adcock, G. T. Houlsby, S. Draper, A. G. Borthwick, Tidal stream energy resource assessment of the Anglesey Skerries, International Journal of Marine Energy 3-4 (2013) e98–e111. doi:10.1016/j.ijome.2013.11.014.

[34] L. E. Myers, A. S. Bahaj, Experimental analysis of the flow field around horizontal axis tidal turbines by use of scale mesh disk rotor simulators, Ocean Engineering 37 (2-3) (2010) 218–227. doi:10.1016/j.oceaneng.2009.11.004.

[35] G. S. Payne, T. J. Stallard, R. Martinez, T. Bruce, Variation of loads on a three-bladed horizontal axis tidal turbine with frequency and blade position, Journal of Fluids and Structures 83 (2018) (2018) 156–170. doi:10.1016/j.jfluidstructs.2018.08.010.

[36] J. McNaughton, Turbulence modelling in the near-field of an axial flow turbine using Code_Saturne, Phd, University of Manchester (2013).

[37] A. Mason-Jones, D. M. O'Doherty, C. E. Morris, T. O'Doherty, Influence of a velocity profile & support structure on tidal stream turbine performance, Renewable Energy 52 (2013) 23–30. doi:10.1016/j.renene.2012.10.022.

[38] U. Ahmed, D. D. Apsley, I. Afgan, T. J. Stallard, P. K. Stansby, Fluctuating loads on a tidal turbine due to velocity shear and turbulence: Comparison of CFD with field data, Renewable Energy 112 (2017) 235–246. doi:10.1016/j.renene.2017.05.048.

[39] R. Martinez, S. Ordonez-Sanchez, M. Allmark, C. Lloyd, C. M. Johnstone, T. O'Doherty, G. Germain, B. Gaurier, Effects on the Loading of Horizontal Axis Turbines when Operating under Wave and Currents., in: Proceedings of the 13th European Wave and Tidal Energy Conference, Napoli, 2019, pp. 1–9.